Final publication is available from Mary Ann Liebert, Inc., publishers https://dx.doi.org/10.1089/ten.tec.2019.0123
Dubois SJ, Kalashnikov N, Moraes C. Robust and Precise Wounding and Analysis of Engineered Contractile Tissues. Tissue Eng Part C Methods. 2019 Nov;25(11):677-686. doi: 10.1089/ten.TEC.2019.0123. Epub 2019 Sep 20. PMID: 31411125.

Robust and Precise Wounding and Analysis of Engineered Contractile Tissues (3D-printed platform for robust, precise puncture and analysis of engineered contractile tissues)

Sarah J. Dubois[1#], Nikita Kalashnikov[1#], Christopher Moraes [1,2,3,*]

[1] Department of Chemical Engineering, McGill University, Montreal, Canada

[2] Department of Biological and Biomedical Engineering, McGill University, Montreal, Canada

[3] Goodman Cancer Research Center, McGill University, Montreal, Canada

# Equal Contributions

* Corresponding author email: chris.moraes@mcgill.ca

Abstract.

Fibrous tissue gap closure is a critically important process initiated in response to traumatic injury. Recent 3D bioengineered models capture cellular details of this process, including wound retraction and closure; but have high failure rates, are labour-intensive, and require considerable expertise to develop and implement with tools that are typically not available in standard wet-labs. Here, we develop a simple and effective 3D-printed wounding platform to reliably create and puncture arrays of pre-stressed tissues and monitor subsequent wound dynamics. We demonstrate the ability to create a range of wound sizes in a contractile collagen/fibroblast tissue, within 125 μm of the desired target location, with high degrees of circularity. Wounds exhibit an initial expansion due to tissue pre-stress, and sufficiently small wounds close completely within 24 hours; while larger wounds initially closed much more rapidly, but did not complete the closure process. Simulating the dynamics of tissue retraction with a viscoplastic finite element model indicates a temporary elevation of circumferential

stresses around the wound edge. Finally, to determine whether active wounding and retraction of the tissue significantly affects closure rates, we compared active puncture of pre-stressed tissue with passive removal of a structure that prevents closure, and found that active wounding and retraction substantially accelerated wound closure when compared to the passive case. Taken together, our findings support the role of active tissue mechanics in wound closure arising from an initial retraction of the tissue. More broadly, these findings demonstrate the utility of the platform and methodology developed here in further understanding the mechanobiological basis for wound closure.

Impact Statement.

In vitro models to study wound formation and closure in pre-stressed tissue are typically challenging to implement. This work provides an easily accessible approach to produce and analyze wounds in arrays of contractile tissues that recapitulate critical features of wound retraction and closure in animal models. The specific modelling and experiments results presented here suggests that mechanobiology effects arising from wound retraction in viscoplastic extracellular matrices could plays an important role in driving wound closure.

1. Introduction

Fibrous tissue gap closure is a fundamental biological process needed for the proper development of various anatomical structures (1,2) such as the neural tube (3,4), heart (5) and palate (6), and for tissue repair and regeneration. Damage to developed tissues initiates hemostasis, inflammation, granulation tissue formation and remodelling, in a precisely orchestrated cascade to heal the wound (7–9). Disrupting this process leads to severe complications, including infection and prolonged inflammation (10–12). Given the complexity of this process in humans and animals, developing *in vitro* models of gap closure is of critical importance in understanding and ultimately manipulating these biological processes.

Existing models of tissue wounding recreate various aspects of the gap closure process. In two-dimensional cultures, scratching cell monolayers with a pipette tip yields considerable insight into gap closure processes (13–17). More advanced approaches such as laser ablation (18,19) may also be used. Alternatively, the wound can be pre-made using stencil (20–23) or tissue patterning techniques (24–26). However, these strategies do not capture the mechanical complexities of a three-dimensional (3D) wound, which may be of critical importance.

3D models of fibrous tissues can be engineered to recreate various stromal tissues (27–30), and these can be adapted for wound models. Wound-like inclusions have been created during fabrication (31–34), but this approach does not capture in vivo-like features of wounding, including retraction of the wound edge in tissues under tension (35). To address these issues, Sakar et al. recently developed a 3D bioengineered wounding model, in which fibroblast-collagen tissues contract around anchoring pillars to form pre-stressed microtissues (36–39) that were then microsurgically injured using a robotically-controlled micromanipulator (40). This model recreates tissue pre-stress, exhibits wound retraction, and closes over time, and provides insight into the mechanics underlying wound closure.

Here, we address technical challenges that limit widespread utility of the model developed by Sakar et al. Their system requires manual micromanipulation of the wounding tool to perform layer-by-layer sequential dissection, using visual feedback. This requires considerable skill and expertise, and would not be scalable for higher-throughput applications, without advanced robotics and control feedback loops that are generally inaccessible in standard wet-labs. To address these issues, we develop a versatile and readily-implemented 3D-printed wounding apparatus, in which arrayed pre-stressed contractile tissues are punctured with a self-aligning array of needles at pre-defined locations. Using this platform, we can rapidly create punctures in pre-stressed tissues at precise locations, and generate wounds in a plate of 24 tissues within one minute. This platform allows us to readily observe wound formation, retraction, and closure; infer mechanical characteristics of the contracted collagen matrix from this data; and demonstrate that tissue retraction mechanically directs future wound closure.

2. Materials and methods

Unless otherwise stated, all cell culture materials and supplies were purchased from Fisher Scientific (Ottawa, ON) and chemicals from Sigma Aldrich (Oakville, ON).

2.1. Tissue wounding platform fabrication

The tissue culture portion of the device containing anchoring micropillars was fabricated using 3D printing, soft lithography and double-replica molding in polydimethylsiloxane (PDMS). Master molds were designed and printed with an Ember 3D printer (Autodesk) in PR57-K Black Prototyping Resin. 3D printed parts were washed in isopropanol, fully cured under a 36W UV light for at least 12 hours, and spray-treated with a mold release agent (Mann Ease Release 200 Agent; Smooth-On; East Texas, PA). PDMS prepolymer (Sylgard 184; Dow Corning) was degassed, loaded and cured at 70^{o}C for 4 hours to produce the negative replica molds. A double replication step was performed, using a passivation layer

of tridecafluoro-1,2,2-tetrahydrooctyle)-1-trichlorosilane (Gelest; Morrisvile, PA) deposited in vapour phase to facilitate release. Fabricated devices were mounted in 6-well plates, cured, and sterilized under UV light for 2 hours. A second device was printed to fit the culture substrate, with positioned holes for wounding needles. Selected needles were mounted in the device, or alternatively, the through-hole can be left open as a guide to insert selected needles when needed.

2.2. Tissue formation and imaging

Human bone marrow fibroblasts (HS-5, ATCC) were used as a model contractile fibroblast cell. HS-5s were cultured in Dulbecco's modified Eagle's medium (DMEM; Gibco), supplemented with 10% fetal bovine serum (FBS) and 1% antibiotic-antimycotic, at 37°C and 5% CO_2. Solubilized collagen (Advanced Biomatrix), 10x DMEM, sodium bicarbonate buffer, and sterile water were mixed following the manufacturer's instructions; and titrated to neutral pH with 1M sodium hydroxide. Trypsinized cells were added at final concentrations of 3 million cells/mL in 1.5 mg/mL collagen. Gels were pipetted into each device, and gelled for 1 hour at 37 °C. Media was added, and the gels contracted over 48 hours around the anchoring pillars. The wounding platform was then positioned using the guide structures, and pressed down to puncture the tissues. At selected time points, tissues were fixed (4% paraformaldehyde, 3 hrs), permeabilized (0.1% Triton-X, 45 mins), labelled (FITC-phalloidin) and/or imaged using brightfield or fluorescent microscopy. Analysis was performed using ImageJ (NIH) to quantify wound area, position and circularity.

2.3. Finite element modelling

To develop estimates of stress patterns surrounding the wound during retraction, a 2D axisymmetric model was implemented in COMSOL (Burlington, MA, USA; model details provided in supplemental information), and the inverse finite element method was used to determine a material model formulation and material parameters that match observations of wound expansion after puncture.

Linear elastic, viscoelastic, and viscoplastic deformation models (parameters in Fig. 4C) were tested using this approach. Briefly, linear elastic and viscoelastic models are described by an elastic modulus E_e, without/with viscous modulus E_v and viscosity μ. The viscoelastic model is extended to incorporate viscoplastic behavior by adding a viscosity term with a yield stress threshold, and a softening function to reduce yield stress under constant material loading (41). Viscoplasticity is described with a linear Norton-Hoff model:

$$\frac{\mathrm{d}\varepsilon_{\mathrm{viscoplastic}}}{\mathrm{d}t} = A\sigma^{n}_{\mathrm{viscoplastic}} = \frac{1}{\mu}\sigma_{\mathrm{viscoplastic}}$$

where the exponent n is set to 1 as per the perfect viscoplastic assumption and the viscoplastic rate coefficient A is selected to be the inverse of viscosity μ. Initial material parameters for these models were obtained from literature sources for mechanical characterization of cell-laden collagen hydrogels (38,42,43,41). For all models, tissue pre-stress is introduced by applying a positive radial displacement boundary condition to match the collagen pull-away distance observed at the micropillars. Tissue wounds are initiated by setting the material properties of a central 'hole' to zero. Further details describing the finite element methods and assumptions applied is available as supplemental information.

3. Results and Discussion

3.1. Fabrication and wounding of pre-stressed tissue arrays

Suspended tissue arrays were fabricated by casting a collagen-cell mixture into a PDMS-based device with integrated anchoring pillars. PDMS devices containing arrays of pillars in square formations (Fig. 1A) were readily fabricated using the described 3D printing / double replica molding process, and were designed to have four 600 μm tall pillars of 500 μm diameter, with center-to-center spacings of 2.5 mm. Contractile tissues were formed by gelling 14 μL of cell-gel solution in each chamber.

Tissues contract over 48 hours to produce a characteristic dense fibrous band around the pillars (Fig. 1B). This dense region arises from free contraction of the unanchored collagen between the edge of the well and the pillars. Central cells pull the collagen tissues towards the tissue center, as evidenced by collagen pull-away from the pillar edges. Simple pillars allowed the tissue to slip over their tips during contraction. 700 μm diameter spheres atop each pillar were large enough to anchor the tissues over 4-5 days, and sufficiently small to allow PDMS release during replica molding.

The wounding platform fit over the tissues using alignment grooves built into the culture device (Fig. 1C). With these grooves to automatically guide box positioning, the wounding array punctured each tissue at pre-defined positions. Manually pressing the structure down was sufficient to align the platform and puncture the tissue (Fig. 1D, E). For all experiments described here, we created wounds in the center of each tissue. Improper wound positioning often leads the development of uneven stresses within the tissue, which can lead to premature tissue failure, and positioning wounds at the center of each tissue avoids this concern. However, wound positioning can also be defined arbitrarily, if needed to answer specific questions that require targeted placement of defects within a tissue. For example, this would be relevant for more complex engineered tissue models that incorporate multiple cell types or advanced structures.

3.2. Characteristic wound dimensions

We empirically found that standard pointed needles often did not create a wound, likely because their tips are thin and relatively rounded, and cause local compaction of the soft collagen tissue. Filing the needles flat (Fig. 2A), and selecting a depth that forces them to penetrate into the underlying PDMS surface reliably produced open wounds as needed. Hence, successful wounding is often accompanied by necessary damage to the underlying PDMS surface.

Needle diameters of 400 to 900 μm (representative images in Fig. 2A) were selected for these studies. The majority of all wounds formed were within 125 μm of the desired location (or 5% of the tissue linear dimension; Fig. 2B). In some cases, wounds were observed within 10% of the desired location, likely due to slight variations in device dimensions arising from PDMS shrinkage during the multiple replica molding steps (44). All wounds produced had circularity shape factors within 10% of a perfect circle, with no significant differences observed based on needle size (Fig. 2C). Wound area was significantly influenced by needle size (Fig. 2D). Interestingly, for small diameter needles, all wounds were larger than the cross-sectional area of the needle, suggesting that the tissue is pulling away or retracting after puncture, as expected in a pre-stressed and physiologically realistic wound model (35). When testing larger needle diameters, although the majority of wounds were larger than the puncturing needle, some were smaller than expected, suggesting incomplete wounding with larger needles. This is likely dependent on the quality of the needle tip, and filing a cookie-cutter edge into larger needles should improve these results.

3.3. Wound closure

Small wounds (< 250 μm) closed within 24-48 hours, while larger wounds (> 750 μm diameter) remained open even 96 hours post-wounding (Fig. 3A, B). We qualitatively examined cell behaviour at the wound edges during closure by fluorescently labelling cells in fixed tissues (Fig. 3C, D), and noticed that "bridging" strings of actin-positive cells formed across the gap in the final stages of closure, consistent with previous studies (40). These qualitative observations demonstrate that the tissue models developed here, despite being significantly larger than existing microtissue models, still capture relevant physiological phenomena during gap closure.

To determine whether wounds size affects closure dynamics in these models closure speeds were analyzed based on initial wound size (Fig. 3E, F). Although larger wounds did not fully close, the initial

closure speeds for wounds > 750μm in diameter were significantly faster than those of smaller wounds (Fig. 3F). Larger wound sizes within this group generally produced faster closure rates (individual data points presented in Supplementary Figure S1). This suggests that distinct closure mechanisms may be activated in large and small wounds. Speculatively, the increased closure rates may be due to mechanical activation of the dense, aligned fibrous tissue band surrounding the anchoring pillars while making large wounds.

In the microtissue models presented by Sarkar et al., the dense collagen bands formed at the tissue periphery constitute a substantial portion of the tissue, and even the smallest wounds alter global tissue dimensions. Since global tissue size also changes during re-establishment of homeostatic tension, the authors conclude that wound closure arises from a combination of global tissue remodelling and local tissue dynamics (Fig. 3G). To determine if this was also true in our system, we compared tissue dimensions in wounded and unwounded models during closure, and found no changes arising from wounding (Fig. 3H). Hence, we can conclude that the present model system provides a sufficiently flexible design space to produce small enough wounds in sufficiently large tissues to effectively decouple local and global remodelling activity, to better understand these distinct processes.

3.4. Analysis of wound edge retraction

Wound edge retraction and stabilization is known to occur when puncturing a pre-stressed tissue, as in animal models (Fig. 4A) (35). Hence, we characterized small wound retraction dynamics in our system. Wounds grew in size for ~20 minutes, and stabilized at 1.4 $\times$ the initial wound area (Fig. 4B). Some heterogeneity was observed, suggesting that variability in tissue mechanics does exist between samples.

We then asked whether our observations of wound retraction could allow us to identify a material model that would provide insight into the mechanical stress patterns surrounding the wound. We developed finite elements analyses for linear, viscoelastic, and viscoplastic materials (Fig. 4C) using

values obtained from literature (38,41–43,45). Linear elastic material models did not exhibit time-dependent retraction, as the wound instantly expanded to release tissue stress. While viscoelastic models did improve upon this and capture time-dependent wound expansion (Fig. 4D), they did not capture the wound expansion magnitude observed experimentally (Fig. 4B). Recently, collagen tissues have been shown to exhibit viscoplastic behaviours (41,43,46–48), and hence we implemented stress-dependent plasticity (Fig. 4C) into our analysis. This material model successfully matched both the magnitude and time-dependency of the wound opening, utilizing parameters similar to those obtained from fundamental mechanical characterization studies of cell-densified collagen (listed in Fig. 4C) (38,42,43,41).

After confirming realistic strain behaviour, we used the viscoplastic simulations to determine whether stress patterns should occur around the wound retraction sites (Fig. 4E, F). Wounding causes immediate reductions in radial stress from the baseline tissue stress levels (2 kPa), and a transient increase in circumferential hoop stress that extends into the surrounding tissue. Viscoplastic deformation dissipates stress over time, but circumferential hoop stress variations remain significant and elevated near the wound for over one hour during and after retraction.

The finite element models presented here do have significant limitations in terms of the precision of predicted stress values. For example, the models are based on material parameters obtained from the literature, and hence do not accurately capture absolute stress levels present in these tissues. The patterns of stress around the wound should remain valid. Furthermore, the model assumes homogenous mechanical properties in the area surrounding the wound tissue, which is quite unlikely given the large area retraction observed which must change local mechanical properties. Hence, these modelling results should only serve to validate that persistent circumferential hoop stress variations arise and are maintained for a long time period after wounding.

3.5. Wound closure dynamics in response to active and passive wounding

To support the hypothesis that mechanical stress developed around the wound during retraction influences closure dynamics, we compared active wounding of a pre-stressed 3D tissue, in which wound retraction is expected, with passive removal of an object that obstructs wound closure (Fig. 5A). This has previously been shown to affect tissue mechanics and closure in 2D systems (51), and our model is uniquely suited to compare these cases. While actively wounded tissues rapidly closed within 24 hours, passively wounded tissues did exhibit signs of wound edge smoothing and closure, but did not close within 48 hours (Fig. 5B). We verified that wound dimensions produced in both models were similar (Fig. 5C), and noted that greater heterogeneity in wound sizes were observed in actively wounded tissues due to variable retraction at the wound edge.

To quantify both retraction and wound closure, we normalized measured wound area to the initial wound. These experiments confirm that passive tissues do not exhibit retraction; while active tissues rapidly retract, and then rapidly close (Fig. 5D). These results strongly suggest that the retraction process itself activates rapid wound closure, perhaps through mechanical activation of cells around the wound. Unlike standard epithelial scratch-based wound closure assays, cell proliferation is unlikely to play a role over these time scales, given the established low proliferation rates of fibroblast cells in 3D matrices (52), and recent findings that cell contractility and not proliferation acts to close wounds in 3D fibrous tissues (40). A mechanical basis for rapid closure is also conceptually consistent with recent studies demonstrating that cells can migrate through a matrix via a slingshot action, in which tension is first built up by tissue deformation, and the elastic energy stored in the matrix can be directed on release of cell adhesion to enhance migration rates (53). Analogously, actively wounding the tissue causes retraction at the wound edge, which increases local matrix density, stiffness, and circumferential

hoop stress (Fig. 3E, F). Speculatively, these factors could act to mechanically activate cells in this region to contract and migrate, thus rapidly closing the gap.

3.6. System utility and limitations

Currently, the contracted collagen system developed by Sakar et al. (40) remains the only in vitro platform to study wounding and recovery in fibrous tissues that capture retraction of the wound edge, a common feature of human and animal model wounds in traumatic injury and developmental morphogenesis. We anticipate that more complex culture systems will be developed based on a pre-stressed tissue, that incorporate epithelial layers, alternative matrix compositions, or multiple cell types. These advanced models would allow investigation into more realistic models of wound healing, including cellular processes such as proliferation, that play a minimal role in fibrous tissue closure, but are more important in epithelial closure mechanisms. The puncture platform developed in this work should be broadly applicable to support these advances, provided that the tissues remain sufficiently soft to allow puncture. The primary limitations associated with this strategy would be around the relative sizing and mechanical characteristics of both the tissue models and the puncturing needle. If the desired wound is too small, a fine needle might simply pierce a low-stress tissue without coring it, allowing it to seal up rapidly much like a rubber septum. Higher levels of tissue stress would force the tissue to spring apart at the wound, addressing this issue. Fine needles may also flex during operation, which could lose wounding efficiency or reduce positional accuracy. While this potential concern may be partially addressed by selecting mechanically rigid materials for the needle, it still presents a fundamental limitation to the minimum wound size possible with this approach.

4. Conclusions

We have developed an easily-implemented and readily accessible tissue engineered model system to study fibrous tissue wounding and closure. The 3D printed system to puncture pre-stressed contractile tissues in pre-defined positions can be constructed with resources that are readily available at most research institutions. Although the system does not provide the spatial resolution of techniques such as microsurgery or laser ablation, the system does significantly improve experimental ease and throughput, affords the capacity to manipulate wound size, and captures key features of wounding and recovery in animal models. The system can be sized appropriately to isolate the effects of local wound healing from global tissue remodelling. Observations of wound retraction in these models provide insight into the mechanical viscoplastic state of the tissue, which suggests that transient mechanical stresses during wound retraction may influence wound closure rates. Taken together these results demonstrate that this simple technological method can be used to further develop insight into this biologically critical process.

Acknowledgements

This project was funded by the Natural Sciences and Engineering Research Council of Canada (NSERC; Discovery RGPIN-2015-05512), the Fonds de recherche du Quebec – Nature et technologies (FRQNT; Grant #205292), and the Canada Research Chairs program in Advanced Cellular Microenvironments to CM. Access to computational modelling software provided by CMC Microsystems. SD and NK gratefully acknowledge support from NSERC and the Eugenie Ulmer Lamothe fund.

Author Disclosure Statement

Authors declare no conflict of interest

Figures

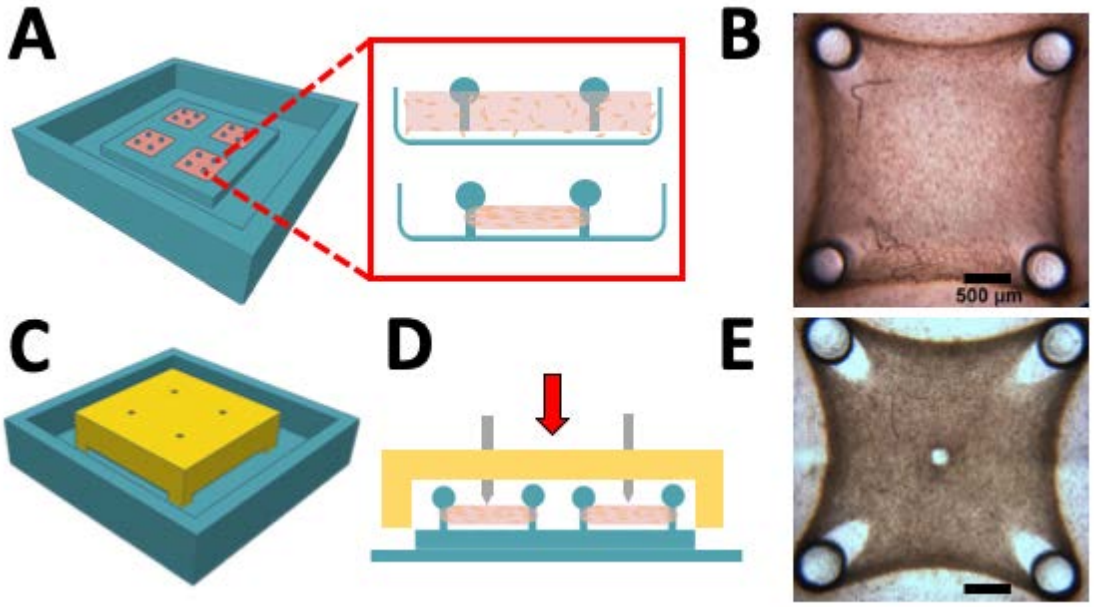

Figure 1. Overview of engineered tissue wounding platform. (A) Schematic overview of tissue culture device operation. Cell laden collagen is loaded into PDMS wells containing replica-molded 3D-printed anchoring pillars, which then contracts to form a pre-stressed tissue suspended between the pillars. (B) Representative brightfield image of pre-stressed tissue (scale bar = 500 µm). (C) Schematic overview of wounding device operation. A 3D printed structure with integrated needles is designed to fit over positioning grooves in the culture substrate, precisely locating the needles at defined locations over the engineered tissues. (D) Manually pressing the wounding platform down creates (E) well-defined and precisely positioned holes in the collagen tissues (scale bar = 500 µm).

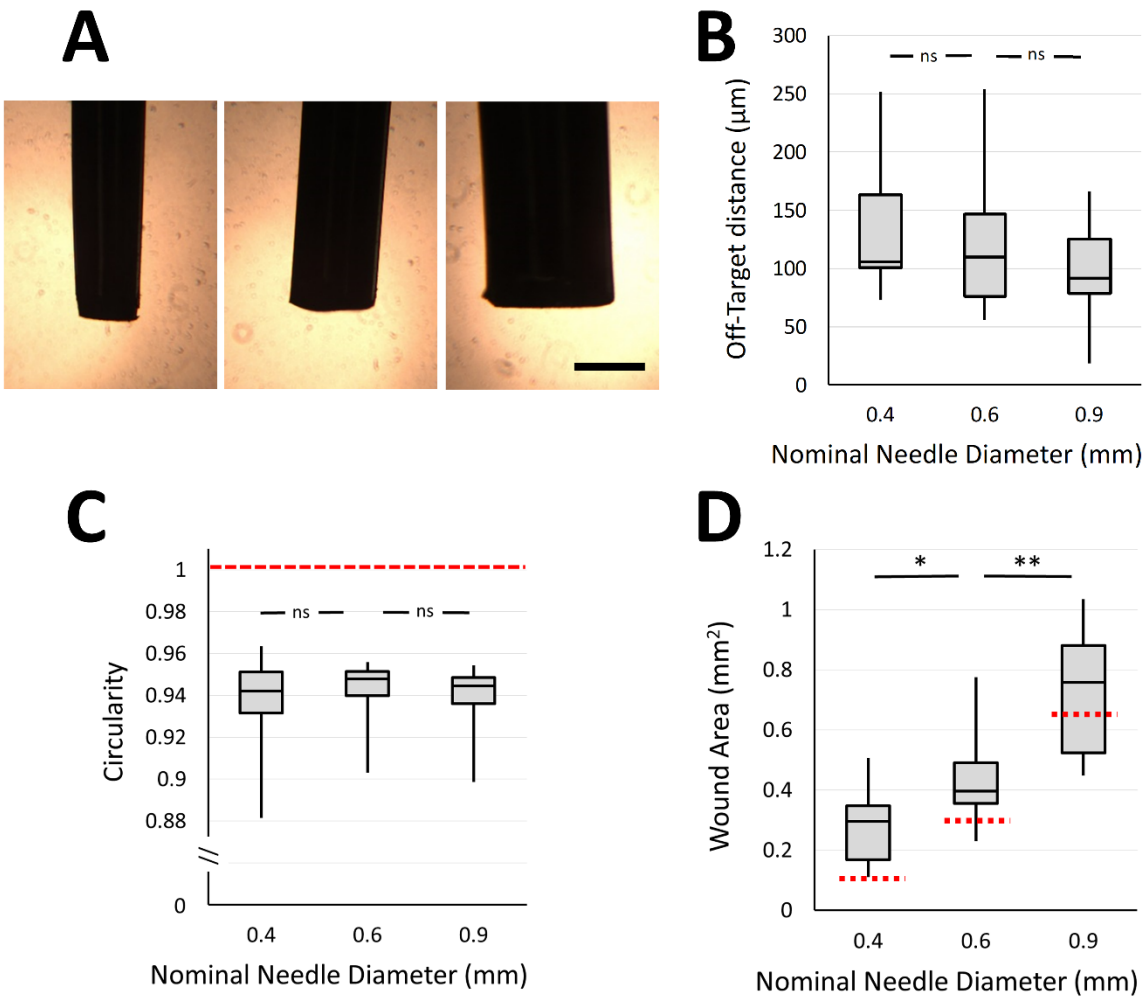

Figure 2. **Characterization of tissue wounding performance.** (A) Brightfield microscopy image of selected punching needles, with nominal diameters of 0.4, 0.6 and 0.9 mm (scale bar = 500 µm). (B) Off-target distance of the wound center from the targeted position. When applied to tissues with lengths of 2500 µm, the majority of wounds are within 5% of their desired positions. (C) Circularity of produced wounds did not vary based on needle size. The red dashed line indicates a perfectly circular wound. (D) Areas of wounds created in the centers of engineered tissues based on selected needle diameters. Red dashed lines represent the expected wound size corresponding to the needle cross-sectional area. All data represented as box plots showing median, interquartile range, and range (n = 11-16; * $p < 0.05$, ** $p < 0.001$, n.s. $p > 0.3$ by two-tailed ANOVA with Tukey post-hoc comparison).

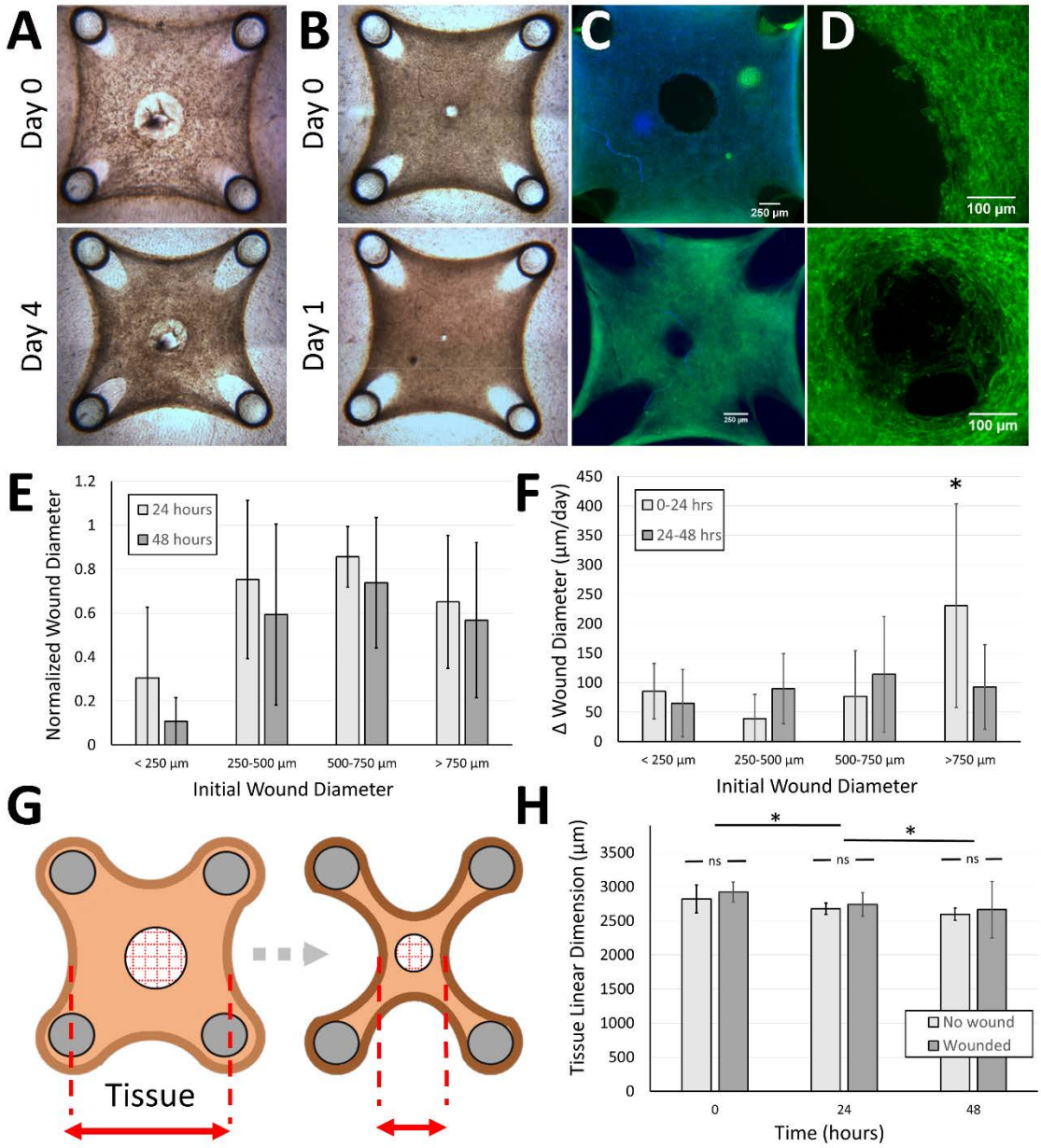

Figure 3. **Wounds and tissue closure characteristics.** (A, B) Representative images of wounded engineered tissues with (A) large and (B) small punctures immediately after wounding and during closure at days 1 and 4. (C, D) Fluorescent micrographs of the (C) wound and (D) wound edge immediately after puncture (top panels), and after 24 hours (bottom panels; green = F-actin). Scale bars = 250 µm for C and 100 µm for D. (E, F) Characteristic wound dimensions over two days of closure for wounds grouped based on initial size, expressed as (E) wound diameter normalized to the initial wound size, and (F) daily change in wound diameter over the 0-24 and 24-48 hour periods after wounding. Data demonstrates that small wound areas close rapidly, but the linear closure rate is similar across days and initial wound size, except for a significant increase in closure rate for the largest wounds tested. (G) Schematic representation of the

potential relationship between changing tissue dimensions and wound closure. Coordinated movement of the whole tissue may assist in wound closure as the tissue continues to contract, and this effect would be influenced by the relative size of the wound compared to the size of the tissue. (H) Comparison of linear tissue dimensions between wounded and unwounded model tissues during further tissue contraction and wound closure. All data reported as mean +/- standard deviation (n = 10-18 in panels E, F, H; * $p < 0.01$, by two-tailed ANOVA with Tukey post-hoc comparisons).

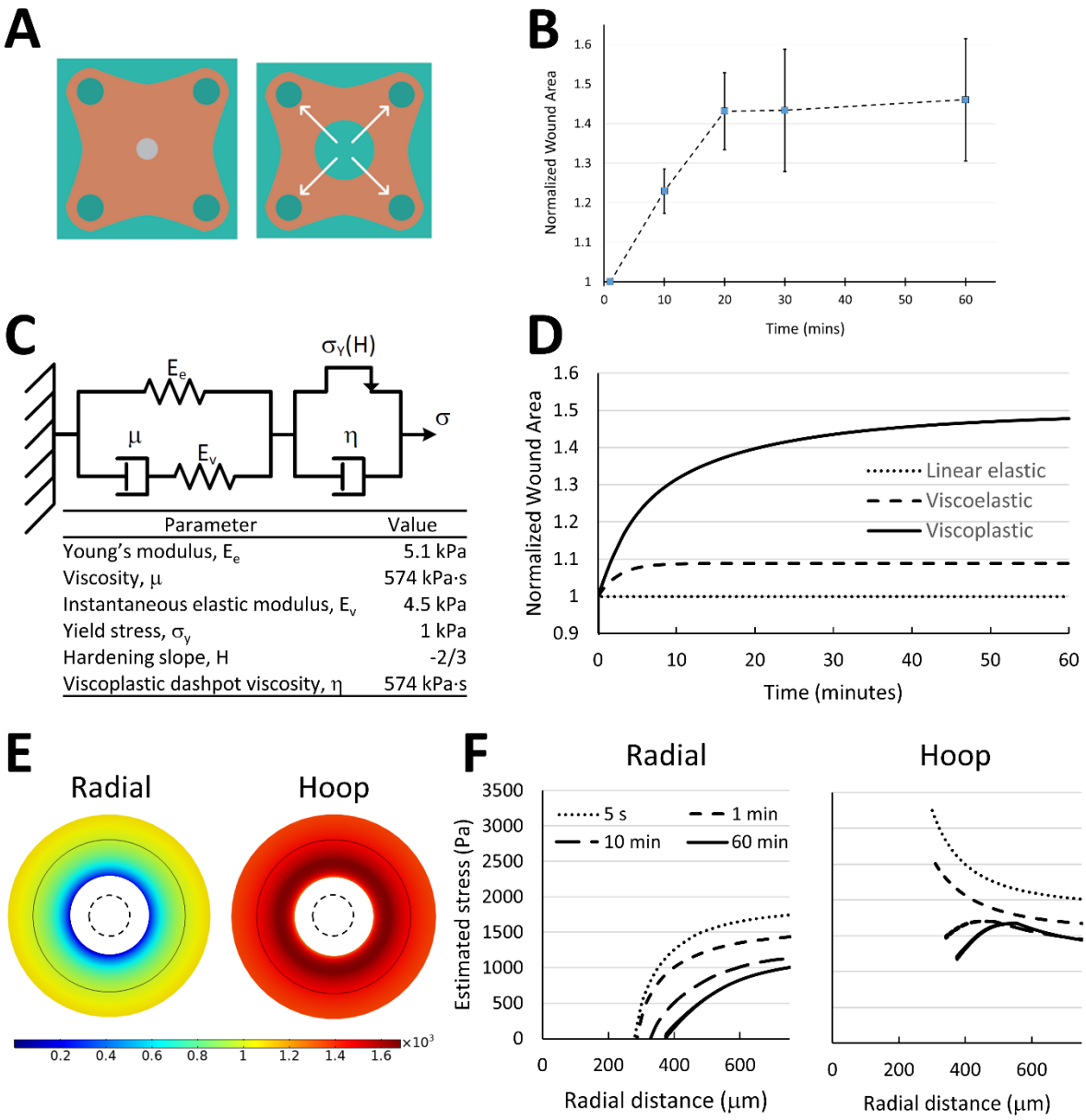

Figure 4. Wound retraction following tissue puncture and associated finite element model. (A) Wound retraction due to tissue pre-stress. (B) Temporal evolution of wound area normalized to initial wound size after tissue puncture. (C) Viscoplastic material model and associated parameters to simulate wound retraction. (D) Comparison of simulated wound retraction for simple linear elastic, viscoelastic and combined viscoplastic models. (E) Characteristic radial and hoop stresses established after complete wound retraction. Dashed lines indicate initial wound size immediately after tissue puncture. (F) Spatial radial and hoop stress profiles within the tissues at steady-state. Wounding causes a reduction in radial stress near the wound edge and a corresponding transient increase in hoop stress. Viscoplastic stress dissipation works over time to attenuate both stress profiles, leaving a characteristic hoop stress peak near the wound.

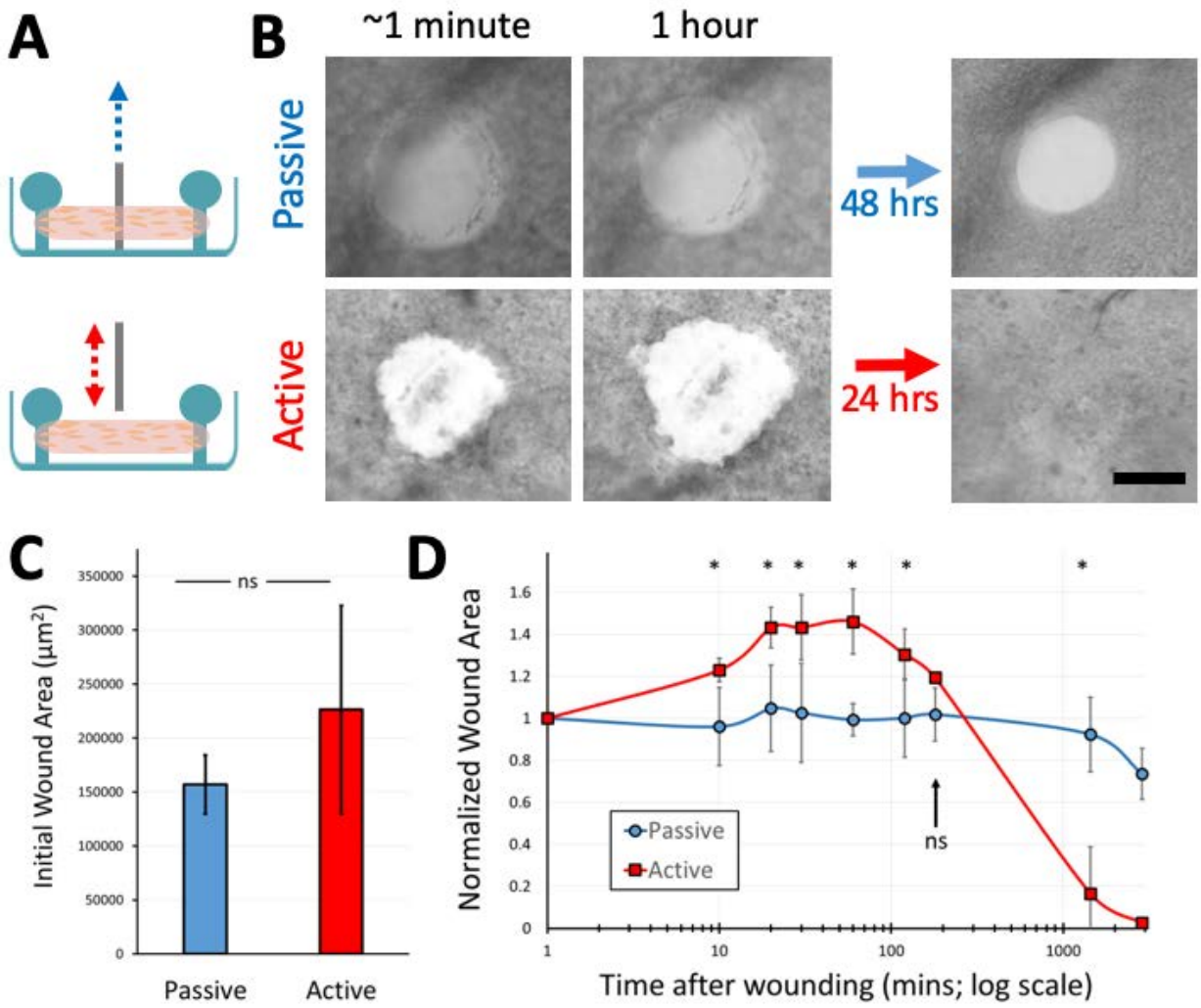

Figure 5. Comparison between passive and active wounding. (A) Tissues were either passively wounded by removing an obstruction from the tissue, or actively wounded with the 3D printed wounding device to achieve small wounds. (B) Passively formed wounds partially closed within 48 hours, but actively formed wounds first expanded and then closed completely within 24 hours (scale bar = 250 µm). (C) No significant differences observed in initial wound area between the passive and active wounding techniques immediately after tissue puncture. (D) Analysis of wound area normalized to initial wound area over time. Passively-generated wounds started to close after 24 hours, while actively formed wounds first expanded over the first 1 hour, and then rapidly closed within 24 hours (n = 4-6, * $p < 0.05$, n.s $p > 0.10$, by two-tailed ANOVA with Tukey post-hoc comparisons).

References

1. Pérez-Pomares JM, Foty RA. Tissue fusion and cell sorting in embryonic development and disease: biomedical implications. BioEssays. **28**(8), 809, 2006;

2. Ray HJ, Niswander L. Mechanisms of tissue fusion during development. Dev. Camb. Engl. **139**(10), 1701, 2012;

3. Ybot-Gonzalez P, Savery D, Gerrelli D, Signore M, Mitchell CE, Faux CH, et al. Convergent extension, planar-cell-polarity signalling and initiation of mouse neural tube closure. Development. **134**(4), 789, 2007;

4. Pyrgaki C, Trainor P, Hadjantonakis A-K, Niswander L. Dynamic imaging of mammalian neural tube closure. Dev. Biol. **344**(2), 941, 2010;

5. Lamers Wouter H., Moorman Antoon F.M. Cardiac Septation. Circ. Res. **91**(2), 93, 2002;

6. Bush JO, Jiang R. Palatogenesis: morphogenetic and molecular mechanisms of secondary palate development. Development. **139**(2), 231, 2012;

7. Martin P. Wound Healing--Aiming for Perfect Skin Regeneration. Science. **276**(5309), 75, 1997;

8. Singer AJ, Clark RAF. Cutaneous Wound Healing. N. Engl. J. Med. **341**(10), 738, 1999;

9. Gurtner GC, Werner S, Barrandon Y, Longaker MT. Wound repair and regeneration. Nature. **453**, 314, 2008;

10. Robson MC. WOUND INFECTION: A Failure of Wound Healing Caused by an Imbalance of Bacteria. Surg. Clin. North Am. **77**(3), 637, 1997;

11. Stadelmann WK, Digenis AG, Tobin GR. Impediments to wound healing. Am. J. Surg. **176**(2, Supplement 1), 39S, 1998;

12. Qian L-W, Fourcaudot AB, Yamane K, You T, Chan RK, Leung KP. Exacerbated and prolonged inflammation impairs wound healing and increases scarring. Wound Repair Regen. **24**(1), 26, 2016;

13. Bement WM, Forscher P, Mooseker MS. A novel cytoskeletal structure involved in purse string wound closure and cell polarity maintenance. J. Cell Biol. **121**(3), 565, 1993;

14. Fenteany G, Janmey PA, Stossel TP. Signaling pathways and cell mechanics involved in wound closure by epithelial cell sheets. Curr. Biol. **10**(14), 831, 2000;

15. Omelchenko T, Vasiliev JM, Gelfand IM, Feder HH, Bonder EM. Rho-dependent formation of epithelial “leader” cells during wound healing. Proc. Natl. Acad. Sci. **100**(19), 10788, 2003;

16. Grasso S, Hernández JA, Chifflet S. Roles of wound geometry, wound size, and extracellular matrix in the healing response of bovine corneal endothelial cells in culture. Am. J. Physiol.-Cell Physiol. **293**(4), C1327, 2007;

17. Liang C-C, Park AY, Guan J-L. *In vitro* scratch assay: a convenient and inexpensive method for analysis of cell migration *in vitro*. Nat. Protoc. **2**(2), 329, 2007;

18. Tamada M, Perez TD, Nelson WJ, Sheetz MP. Two distinct modes of myosin assembly and dynamics during epithelial wound closure. J. Cell Biol. **176**(1), 27, 2007;

19. Brugués A, Anon E, Conte V, Veldhuis JH, Gupta M, Colombelli J, et al. Forces driving epithelial wound healing. Nat. Phys. **10**(9), 683, 2014;

20. Poujade M, Grasland-Mongrain E, Hertzog A, Jouanneau J, Chavrier P, Ladoux B, et al. Collective migration of an epithelial monolayer in response to a model wound. Proc. Natl. Acad. Sci. **104**(41), 15988, 2007;

21. Anon E, Serra-Picamal X, Hersen P, Gauthier NC, Sheetz MP, Trepat X, et al. Cell crawling mediates collective cell migration to close undamaged epithelial gaps. Proc. Natl. Acad. Sci. **109**(27), 10891, 2012;

22. Cochet-Escartin O, Ranft J, Silberzan P, Marcq P. Border Forces and Friction Control Epithelial Closure Dynamics. Biophys. J. **106**(1), 65, 2014;

23. Ravasio A, Cheddadi I, Chen T, Pereira T, Ong HT, Bertocchi C, et al. Gap geometry dictates epithelial closure efficiency. Nat. Commun. **6**, 7683, 2015;

24. Vedula SRK, Hirata H, Nai MH, Brugués A, Toyama Y, Trepat X, et al. Epithelial bridges maintain tissue integrity during collective cell migration. Nat. Mater. **13**(1), 87, 2014;

25. Nier V, Deforet M, Duclos G, Yevick HG, Cochet-Escartin O, Marcq P, et al. Tissue fusion over nonadhering surfaces. Proc. Natl. Acad. Sci. **112**(31), 9546, 2015;

26. Vedula SRK, Peyret G, Cheddadi I, Chen T, Brugués A, Hirata H, et al. Mechanics of epithelial closure over non-adherent environments. Nat. Commun. **6**, 6111, 2015;

27. Bell E, Ivarsson B, Merrill C. Production of a tissue-like structure by contraction of collagen lattices by human fibroblasts of different proliferative potential in vitro. Proc. Natl. Acad. Sci. **76**(3), 1274, 1979;

28. Moraes C, Simon AB, Putnam AJ, Takayama S. Aqueous two-phase printing of cell-containing contractile collagen microgels. Biomaterials. **34**(37), 9623, 2013;

29. Carlson MA, Longaker MT. The fibroblast-populated collagen matrix as a model of wound healing: a review of the evidence. Wound Repair Regen. **12**(2), 134, 2004;

30. Leung BM, Moraes C, Cavnar SP, Luker KE, Luker GD, Takayama S. Microscale 3D Collagen Cell Culture Assays in Conventional Flat-Bottom 384-Well Plates. J. Lab. Autom. **20**(2), 138, 2015;

31. Safferling K, Sütterlin T, Westphal K, Ernst C, Breuhahn K, James M, et al. Wound healing revised: A novel reepithelialization mechanism revealed by in vitro and in silico models. J Cell Biol. **203**(4), 691, 2013;

32. Chen ZJ, Yang JP, Wu BM, Tawil B. A Novel Three-Dimensional Wound Healing Model. J. Dev. Biol. **2**(4), 198, 2014;

33. Price BL, Lovering AM, Bowling FL, Dobson CB. Development of a Novel Collagen Wound Model To Simulate the Activity and Distribution of Antimicrobials in Soft Tissue during Diabetic Foot Infection. Antimicrob. Agents Chemother. **60**(11), 6880, 2016;

34. Ottosson M, Jakobsson A, Johansson F. Accelerated Wound Closure - Differently Organized Nanofibers Affect Cell Migration and Hence the Closure of Artificial Wounds in a Cell Based In Vitro Model. PLOS ONE. **12**(1), e0169419, 2017;

35. Davidson JM. Animal models for wound repair. Arch. Dermatol. Res. **290 Suppl**, S1, 1998;

36. Legant WR, Pathak A, Yang MT, Deshpande VS, McMeeking RM, Chen CS. Microfabricated tissue gauges to measure and manipulate forces from 3D microtissues. Proc. Natl. Acad. Sci. **106**(25), 10097, 2009;

37. Legant WR, Chen CS, Vogel V. Force-induced fibronectin assembly and matrix remodeling in a 3D microtissue model of tissue morphogenesis. Integr. Biol. **4**(10), 1164, 2012;

38. Wang H, Svoronos AA, Boudou T, Sakar MS, Schell JY, Morgan JR, et al. Necking and failure of constrained 3D microtissues induced by cellular tension. Proc. Natl. Acad. Sci. **110**(52), 20923, 2013;

39. Ramade A, Legant WR, Picart C, Chen CS, Boudou T. Chapter 13 - Microfabrication of a Platform to Measure and Manipulate the Mechanics of Engineered Microtissues. In: Piel M, Théry M, editors. Methods Cell Biol. [Internet]. Academic Press; p. 191–211, 2014 [cited 2019 Apr 10]. Available from: http://www.sciencedirect.com/science/article/pii/B9780128002810000130

40. Sakar MS, Eyckmans J, Pieters R, Eberli D, Nelson BJ, Chen CS. Cellular forces and matrix assembly coordinate fibrous tissue repair. Nat. Commun. **7**, ncomms11036, 2016;

41. Malandrino A, Trepat X, Kamm RD, Mak M. Dynamic filopodial forces induce accumulation, damage, and plastic remodeling of 3D extracellular matrices. PLOS Comput. Biol. **15**(4), e1006684, 2019;

42. Feng Z, Seya D, Kitajima T, Kosawada T, Nakamura T, Umezu M. Viscoelastic characteristics of contracted collagen gels populated with rat fibroblasts or cardiomyocytes. J. Artif. Organs. **13**(3), 139, 2010;

43. Liu AS, Wang H, Copeland CR, Chen CS, Shenoy VB, Reich DH. Matrix viscoplasticity and its shielding by active mechanics in microtissue models: experiments and mathematical modeling. Sci. Rep. **6**, 33919, 2016;

44. Moraes C, Sun Y, Simmons CA. Solving the shrinkage-induced PDMS alignment registration issue in multilayer soft lithography. J. Micromechanics Microengineering. **19**(6), 065015, 2009;

45. Raub CB, Suresh V, Krasieva T, Lyubovitsky J, Mih JD, Putnam AJ, et al. Noninvasive Assessment of Collagen Gel Microstructure and Mechanics Using Multiphoton Microscopy. Biophys. J. **92**(6), 2212, 2007;

46. Nam S, Lee J, Brownfield DG, Chaudhuri O. Viscoplasticity Enables Mechanical Remodeling of Matrix by Cells. Biophys. J. **111**(10), 2296, 2016;

47. Ban E, Franklin JM, Nam S, Smith LR, Wang H, Wells RG, et al. Mechanisms of Plastic Deformation in Collagen Networks Induced by Cellular Forces. Biophys. J. **114**(2), 450, 2018;

48. Wisdom KM, Adebowale K, Chang J, Lee JY, Nam S, Desai R, et al. Matrix mechanical plasticity regulates cancer cell migration through confining microenvironments. Nat. Commun. **9**(1), 4144, 2018;

49. Sniadecki NJ, Anguelouch A, Yang MT, Lamb CM, Liu Z, Kirschner SB, et al. Magnetic microposts as an approach to apply forces to living cells. Proc. Natl. Acad. Sci. **104**(37), 14553, 2007;

50. Bement WM, Mandato CA, Kirsch MN. Wound-induced assembly and closure of an actomyosin purse string in Xenopus oocytes. Curr. Biol. **9**(11), 579, 1999;

51. Murrell M, Kamm R, Matsudaira P. Tension, Free Space, and Cell Damage in a Microfluidic Wound Healing Assay. PLOS ONE. **6**(9), e24283, 2011;

52. de la Puente P, Quan N, Hoo RS, Muz B, Gilson RC, Luderer M, et al. Newly established myeloma-derived stromal cell line MSP-1 supports multiple myeloma proliferation, migration, and adhesion and induces drug resistance more than normal-derived stroma. Haematologica. **101**(7), e307, 2016;

53. Wang WY, Davidson CD, Lin D, Baker BM. Actomyosin contractility-dependent matrix stretch and recoil induces rapid cell migration. Nat. Commun. **10**(1), 1186, 2019;

54. Babaei B, Velasquez-Mao AJ, Pryse KM, McConnaughey WB, Elson EL, Genin GM. Energy dissipation in quasi-linear viscoelastic tissues, cells, and extracellular matrix. J. Mech. Behav. Biomed. Mater. **84**, 198, 2018;

Supplementary Information – Finite Element Modelling

Modelling objectives and challenges. Our primary goal in implementing these models is to provide a first-order estimate of the local stress patterns surrounding the wound, using a reasonably-parameterized material model that provides consistent results with our observations of retraction. We first considered a rigorous mechanical characterization approach, but realized that this is extremely challenging in the present system. First, the mechanical properties of cell-contracted collagen gels are quite complex, as cell-driven remodelling significantly alters rate-dependent mechanical properties (Babaei et al., 2018). The material properties would hence be cell-type, cell density, and culture-condition dependent; and detailed mechanical characterization studies would be required at multiple time points during tissue contraction and wound retraction. Second, the micropillar-anchored contractile tissues developed here are relatively small and exhibit spatial heterogeneity between the tissue edges and center. This precludes the use of standard uniaxial, multiaxial and shear testing methods, which would not be able to isolate the mechanical properties of the tissue immediately surrounding the wound. The low tissue stiffness also precludes the use of nanoindentation or atomic force microscopy mapping techniques, with relatively limited force resolution or stroke lengths. Hence, developing a model based on experimental characterization would require the development of novel techniques and complex model formulations, beyond the scope of this present work.

Inverse finite element modelling strategy. To obtain a qualitative idea of the mechanical stresses that are present during wound retraction, we propose an inverse finite element modelling approach, in which we initialize the material formulations and parameters using data provided in the literature, and then tune these parameters within a reasonable range by iteratively modifying them to match observations of wound retraction. We first evaluate the behaviour of three material models that have previously been used to model collagen (linear elastic, viscoelastic, and viscoplastic), to determine which formulation would best capture the observed areal wound increase of ~40% that develops over ~20 minutes (Figure 4B). Because this strategy is not based upon a force measurement or mechanical characterization, we cannot conclude the absolute levels of stress within the tissue, but these optimized parameters should provide reasonable insight into the stress patterns surrounding the wound.

Material formulations. Linear elastic models where characterized by a simple elastic modulus E_e (Malandrino et al., 2019). Viscoelastic behaviour was modelled with a standard Maxwell spring/dashpot combination in parallel with the elastic spring element. The stress strain behaviour of the Maxwell arm is determined by the instantaneous elastic modulus E_v and viscosity μ of the dashpot (Feng et al., 2010). Viscoplastic behavior is introduced by adding a viscosity term with a yield stress threshold, and a linear softening function to reduce yield stress under constant loading (Fig. 4C). Viscoplasticity is hence described with a linear Norton-Hoff model:

$$\frac{\mathrm{d}\varepsilon_{\mathrm{viscoplastic}}}{\mathrm{d}t} = A\sigma^{n}_{\mathrm{viscoplastic}} = \frac{1}{\mu}\sigma_{\mathrm{viscoplastic}}$$

where the exponent n is set to 1 as per the perfect viscoplastic assumption and the viscoplastic rate coefficient A is selected to be the inverse of viscosity μ (Malandrino et al., 2019).

Geometry. The finite element geometry and boundary conditions were developed based on our observations that tissue dimensions did not change with wounding (Figure 3H). This indicates that the displacements caused by wounds do not translate to the tissue edge, and allowed us to assume that modelling the central tissue region was sufficient to capture the relevant wound expansion dynamics. Therefore, we neglected the "arms" of the tissue construct. To further simplify our analysis, we assumed that the central region can be represented with a spatially homogenous material model formulation, based on microscopy images showing two distinct regions of the tissue: the thick banded edge, and the central relatively region with comparatively low cell density. Hence, we modeled the tissue as a single material with a 2D axisymmetric geometry of radius 750 µm and thickness of 1mm (based on microscopy observations). We formed this axisymmetric disc from two concentric sections, so that we could initiate "wounding" at t = 0 by setting the material properties of the central 'hole' section to zero.

Boundary Conditions. An anchored collagen tissue that has been contracted by cells must be under some level of pre-stress prior to wounding. We captured pre-stress in our finite element models by applying a positive radial displacement boundary condition to the outer edge of the circle. To estimate an appropriate displacement, we approximated the size of the pull-away region between the tissue and the anchoring pillar, and used this number to apply a radial strain of 33%. This strain-based approach to determine prestress neglects any changes to tissue material properties during contraction, and is hence not entirely accurate; but is similar in stress magnitude (1.65 kPa to 2 kPa depending on material model selected) to scaled measurements of tissue stress made by others, including Sakar et al. who used deflection of PDMS micropillars to determine tissue stress.

Model meshing. We initially set the mesh to be very fine near the boundary of the hole domain (2 µm), where stresses and strains are expected to be much higher. We then conducted a mesh-size sensitivity analysis and reduced the mesh size throughout the tissue domain, and saw no significant differences in computed stresses and strains for a mapped quad element size set to 1% of the total microtissue length, which ensured that the coefficient of variation was less than 1%. Mesh element quality was maintained above 0.9. Hence, all reported data was obtained using this optimized mesh size.

Material parameters. The model parameters used, their literature sources and the final parameters obtained from the iterative inverse finite element approach have been summarized as follows:

Linear Elastic **Reference /** ***Method***	**Parameter**	**Literature values**	**Lower bound tested**	**Upper bound tested**	**Result**	**Value used for demo curve (Fig 4D)**
Raub et al., 2007 / *Parallel Plate Rheometry on cell-collagen gels*	Elastic modulus (E_e)	1 - 10 kPa	0.01 kPa	100 kPa	Does not capture time-dependency	5.1 kPa

Viscoelastic **Reference /** ***Method***	**Parameter**	**Literature values**	**Lower bound tested**	**Upper bound tested**	**Result**	**Value used for demo curve (Fig. 4D)**
Feng et al., 2010 / *Custom-made uniaxial testing on fibroblast-laden collagen gels*	Elastic modulus (E_e)	5.1 kPa	0.01 kPa	100 kPa	n/a	5.1 kPa
Feng et al., 2010	Instantaneous elastic modulus (E_v)	4.5 kPa	500 Pa	50 kPa	Unable to capture large area expansion	4.5 kPa
Feng et al., 2010	Viscosity (μ)	143.6 kPa·s	10 kPa·s	1000 kPa·s	Unable to capture slow expansion times	143.6 kPa·s

Viscoplastic Parameters **Reference /** ***Method***	**Parameter**	**Literature values**	**Empirical best fit to data (used in Fig 4D, F)**
Malandrino et al. 2019 / *Confocal imaging of collagen fibril deformation*	Yield stress	0.3 kPa	1 kPa
Malandrino et al. (2019)	Hardening function	-2/3	-2/3
Malandrino et al. (2019)	Viscoplastic dashpot viscosity	100 kPa·s	574 kPa·s

Comparison and selection of material models. Unsurprisingly, the linear elastic model did not match our experimental observations of slow wound expansion, as it has no time-dependent term. The standard linear solid viscoelastic model with parameters obtained from Feng et al. (2010) did introduce a time-dependent wound expansion, but was unable to capture the areal magnitude (40% increase) and long time scales (~20 minutes) observed experimentally, even when adjusting the model parameters by over one order of magnitude away from published results. Numerous recent studies have demonstrated that cell-laden collagen exhibits viscoplastic material behavior (Liu et al., 2016; Nam et al., 2016; Malandrino et al., 2019), and introducing a viscoplastic element successfully captured the requisite large area wound expansion over long time scales. Hence the viscoplastic model was selected as best capturing the dynamics of wound expansion, and used to estimate the local stress patterns around the wound (Fig. 4F).

Supplementary Figures

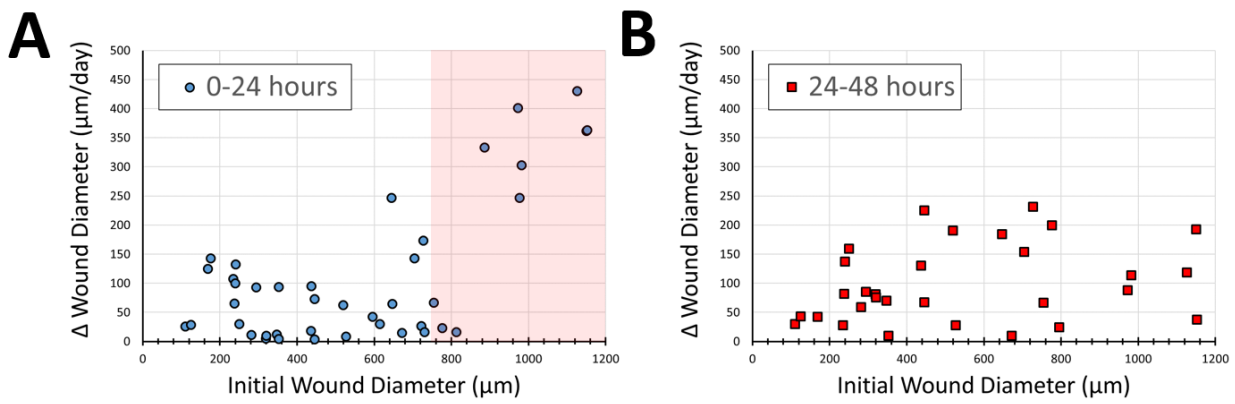

Supplementary Figure S1. Individual datapoints for the statistical comparison presented in Figure 3F. (A, B) Daily wound closure rates for various initial wound diameters over (A) 0-24 hours and (B) 24-48 hours after wounding. The pink highlighted region demonstrates the group of data points that are statistically significant compared to the other groups in this comparison.

Supplementary References

Babaei B, Velasquez-Mao AJ, Pryse KM, McConnaughey WB, Elson EL, Genin GM. Energy dissipation in quasi-linear viscoelastic tissues, cells, and extracellular matrix. J. Mech. Behav. Biomed. Mater. **84**, 198, 2018

Raub CB, Suresh V, Krasieva T, Lyubovitsky J, Mih JD, Putnam AJ, et al. Noninvasive Assessment of Collagen Gel Microstructure and Mechanics Using Multiphoton Microscopy. Biophys. J. **92**(6), 2212, 2007

Feng Z, Seya D, Kitajima T, Kosawada T, Nakamura T, Umezu M. Viscoelastic characteristics of contracted collagen gels populated with rat fibroblasts or cardiomyocytes. J. Artif. Organs. **13**(3), 139, 2010

Malandrino A, Trepat X, Kamm RD, Mak M. Dynamic filopodial forces induce accumulation, damage, and plastic remodeling of 3D extracellular matrices. PLOS Comput. Biol. **15**(4), e1006684, 2019;